Chiral Skyrmion and Skyrmionium States Engineered by the Gradient of Curvature

Oleksandr V. Pylypovskyi,[1,*] Denys Makarov,[2] Volodymyr P. Kravchuk,[3,4] Yuri Gaididei,[3] Avadh Saxena,[5] and Denis D. Sheka[1]

[1] *Taras Shevchenko National University of Kyiv, 01601 Kyiv, Ukraine*

[2] *Helmholtz-Zentrum Dresden-Rossendorf e.V., Institute of Ion Beam Physics and Materials Research, 01328 Dresden, Germany*

[3] *Bogolyubov Institute for Theoretical Physics of National Academy of Sciences of Ukraine, 03680 Kyiv, Ukraine*

[4] *Leibniz-Institut für Festkörper- und Werkstoffforschung, IFW Dresden, D-01171 Dresden, Germany*

[5] *Theoretical Division, Los Alamos National Laboratory, Los Alamos, New Mexico 87545, USA*

(Received 10 July 2018; revised manuscript received 7 November 2018; published 26 December 2018)

Curvilinear nanomagnets can support magnetic skyrmions stabilized at a local curvature without any intrinsic chiral interactions. Here, we propose an alternative mechanism to stabilize chiral Néel skyrmion states relying on the gradient of curvature. We illustrate our approach with an example of a magnetic thin film with perpendicular magnetic anisotropy shaped as a circular indentation. We show that in addition to the topologically trivial ground state, there are two skyrmion states with winding numbers ± 1 and a skyrmionium state with a winding number 0. These chiral states are formed due to the pinning of a chiral magnetic domain wall at a bend of the nanoindentation due to spatial inhomogeneity of the curvature-induced Dzyaloshinskii-Moriya interaction. The latter emerges due to the gradient of the local curvature at the bend. While the chirality of the skyrmion is determined by the sign of the local curvature, its radius can be varied in a broad range by engineering the position of the bend with respect to the center of the nanoindentation. We propose a general method, which enables us to reduce the magnetic problem for any surface of revolution to the common planar problem by means of proper modification of constants of anisotropy and Dzyaloshinskii-Moriya interaction.

DOI: 10.1103/PhysRevApplied.10.064057

I. INTRODUCTION

Chiral magnetic textures such as domain walls, skyrmions, and skyrmion bubbles are considered as promising building blocks for prospective memory and logic devices relying on spintronics and spinorbitronics concepts [1–4]. There is intensive work not only on the controlled creation of these topologically nontrivial objects [4–9] but also on the manipulation of their static and dynamic properties [4,5,10–13]. Primarily, most of such activities are dedicated to flat magnetic thin films with perpendicular magnetic anisotropy. At the same time, sample geometry can significantly alter statics and dynamics of magnetic textures [14–18]. Recently, it was shown that local curvature can lead to the emergent magnetostatically driven chiral effects that are nonlocal [17–24], but also to the appearance of exchange-driven Dzyaloshinskii-Moriya interaction (DMI) [25,26]. The latter enables a route to realize skyrmions [27] and field-free skyrmion lattices as a ground state [28].

Here, we demonstrate that, even in the absence of an intrinsic DMI, the gradient of the local curvature is an efficient means to stabilize chiral localized magnetic objects, allowing us to manipulate their size at will. We emphasize the physical mechanism of the effect to be the pinning of a chiral magnetic domain wall on an inhomogeneity of the geometry-driven DMI localized at the bend of a ferromagnetic nanomembrane. Engineering the geometry of a circular nanoindentation [Fig. 1(a)] to have a defined curvature and distance between bends allows one to form chiral objects with winding numbers Q of ± 1 and 0. Considering their topological properties, we refer to the objects with $Q = \pm 1$ as skyrmion states and 0 as the skyrmionium state [29,30]. The diameter of a skyrmion is determined by the diameter of the circular base of the nanoindentation. The developed theoretical formalism allows one to transfer the conclusions to flat systems with spatially inhomogeneous DMI. In this respect, we propose an alternative mechanism of pinning of the magnetic domain walls on gradients of DMI in a film.

*engraver@knu.ua

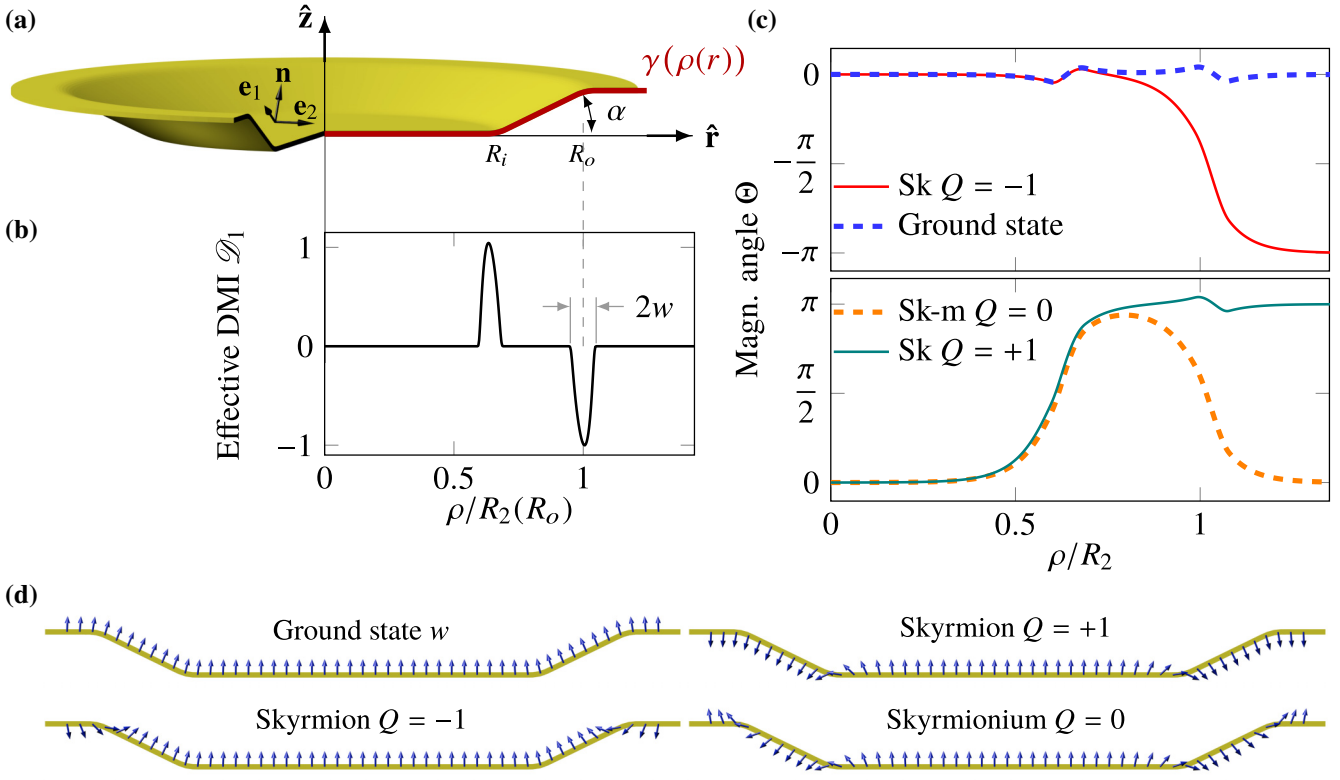

FIG. 1. Sample geometry and magnetization patterns. (a) Circular nanoindentation with inner radius $R_i = 10$, outer radius $R_o = 15$, and bending angle $\alpha = 26^\circ$ (curvature amplitude $\varkappa_0 = 0.5$ and curvature half-width $w = 0.75$; see Appendix C for details). A local basis is given by radial, polar, and normal unit vectors $\{\mathbf{e}_1, \mathbf{e}_2, \mathbf{n}\}$, and the cone angle equals $\pi - \alpha$. (b) The effective DMI coefficient $\mathscr{D}_1$ plotted as function of ρ; see Eq. (B14b). (c) Equilibrium states: the topologically trivial ground state and three types of skyrmions of different chiralities (winding number $Q = \pm 1$) and a topologically trivial skyrmionium state ($Q = 0$). (d) Magnetization distribution for states shown in (c).

II. RESULTS

A. Model

We consider a thin three-dimensional (3D) curved magnetic nanomembrane of thickness h with uniaxial, locally perpendicular anisotropy in the absence of an intrinsic DMI. The nanomembrane is curved in a way to form a circular nanoindentation [Fig. 1(a)], where $\hat{\mathbf{z}}$ and $\hat{\mathbf{r}}$ are introduced as longitudinal and radial axes, respectively.

A magnetic texture is controlled by three interactions: exchange, requiring uniform magnetization in the laboratory reference frame; anisotropy, tracking the nanomembrane curvature; and local magnetostatics with the total energy

$$E = h \int \left[A\mathscr{E}_{\text{ex}} - K_u m_n^2 - \frac{M_S}{2} (\mathbf{m} \cdot \mathbf{H}_d) \right] dS, \qquad (1)$$

where A is the exchange stiffness, K_u is the intrinsic anisotropy along the normal $\mathbf{n}$ to the surface, M_S is saturation magnetization, and $\mathbf{H}_d$ is the demagnetizing field. The competition between the exchange and other energy contributions in Eq. (1) results in the characteristic magnetic length $\ell = \sqrt{A/K}$ with the effective anisotropy coefficient $K = K_u - 2\pi M_S^2$. The latter incorporates any intrinsic anisotropy K_u along the normal $\mathbf{n}$ to the surface and local magnetostatics in the thin-film limit $h \lesssim \ell$ [31–34]; see also Eq. (1). Here, we limit ourselves to the local magnetostatic contribution only, which works well for thin films [27,28,35] and the effects of nonlocal magnetostatics will be studied in a separate work. Below we will measure all lengths in units of ℓ.

The nanoindentation geometry is defined in the cylindrical reference frame (r, χ, z) by the revolution of a curve $\boldsymbol{\gamma}(r) = r\hat{\mathbf{r}} + z(r)\hat{\mathbf{z}}$ around the $\hat{\mathbf{z}}$ axis. The curve $\boldsymbol{\gamma}$ generates a surface $\varsigma = \varsigma(r, \chi)$; see Fig. 1(a) and Appendix A for details. It represents a conic frustum indentation with an inner radius $r = R_i$ and an outer radius $r = R_o$. We will characterize ς through its two principal curvatures $\varkappa_1(r)$ and $\varkappa_2(r)$, where $\varkappa_1$ is the normal curvature of the generatrix $\boldsymbol{\gamma}$.

Surfaces of revolution support radially symmetric magnetization textures $\mathbf{m}(r) = \sin\Theta\mathbf{e}_1 + \cos\Theta\mathbf{n}$; see Appendix B for details. Here, the local orthonormal reference frame $\{\mathbf{e}_1, \mathbf{e}_2, \mathbf{n}\}$ is used with $\mathbf{e}_1$ being the unit

vector along the generatrix $\mathbf{e}_2 = \mathbf{n} \times \mathbf{e}_1$ and $\Theta = \Theta(r) \in \mathbb{R}$.

To compare topologically nontrivial magnetization textures in flat and curvilinear samples, it is instructive to project $\boldsymbol{\varsigma}$ to a plane in such a way as to reconstruct a planar skyrmion equation; see, e.g., Eq. (13) from Ref. [36]. We note that not every transformation will allow such reconstruction. The only transformation that provides this possibility is

$$\rho(r) = r \exp \int_r^\infty \left[1 - \sqrt{1 + \left(\frac{dz}{d\zeta} \right)^2} \right] \frac{d\zeta}{\zeta}. \tag{2}$$

See Appendix B for details. Here, we introduce a surface polar coordinate ρ, which allows us to obtain the same structure of the total energy density and equation as in the planar case. Nanomembrane bends in new coordinates are located at $\rho(R_i) = R_1$ and $\rho(R_o) = R_2$. In the surface polar reference frame, the total energy density resembles the energy of a planar film with exchange, anisotropy, and Dzyaloshinskii-Moriya interactions:

$$\mathscr{E} = \underbrace{\Theta'^2 + \frac{\sin^2\Theta}{\rho^2}}_{\text{exchange}} + \underbrace{\mathscr{K} \sin^2\Theta}_{\text{anisotropy}} - \underbrace{\mathscr{D}_1 \Theta'}_{\text{DMI 1}} - \underbrace{\mathscr{D}_2 \frac{\sin\Theta\cos\Theta}{\rho}}_{\text{DMI 2}}, \tag{3}$$

with prime denoting the derivative with respect to ρ. However, instead of the typical planar magnet, all strengths of emergent interactions for the curved nanomembrane become coordinate dependent. In particular, coefficients of geometrically induced DMI are determined by local curvatures, $\mathscr{D}_i \propto \varkappa_i$, $i = 1, 2$; see Appendix B for details. They vanish in the flat region of the membrane: the coefficient $\mathscr{D}_1$ is nonzero only in the bend regions of the generatrix $\boldsymbol{\gamma}$ and $\mathscr{D}_2$ appears only in the inclined part of the indentation. While $\varkappa_1$ can assume an arbitrary value and is given by the generatrix bend parameters only, $\varkappa_2 \propto 1/r$. The effective anisotropy $\mathscr{K}$ is determined by $\varkappa_2$ and the ratio r/ρ. An example of the spatial dependence of $\mathscr{D}_1$ is shown in Fig. 1(b).

The Euler equation for the energy functional [Eq. (3)] determines an equilibrium radially symmetric magnetization texture, described by a forced skyrmion equation,

$$\Theta'' + \frac{\Theta'}{\rho} - \frac{\sin 2\Theta}{2}\left(\mathscr{K} + \frac{1}{\rho^2} \right) - \mathscr{D}_2 \frac{\sin^2\Theta}{\rho} = f(\rho), \tag{4a}$$

where

$$f(\rho) = \frac{\mathscr{D}_1 - \mathscr{D}_2}{2\rho} + \frac{1}{2}\mathscr{D}_1' = \frac{r(\rho)}{\rho}(\varkappa_1 + \varkappa_2)'. \tag{4b}$$

The effective anisotropy $\mathscr{K}$ and DMI $\mathscr{D}_2$ in Eq. (4a) are functions of the coordinate ρ. In the case $\mathscr{K} = \text{const}$, $\mathscr{D}_2 = \text{const}$, and $f(\rho) = 0$, Eq. (4) is reduced to a typical skyrmionlike equation [5,36–38]. A comparison with this limiting case points out an analogy between the flat and curvilinear skyrmions. At the same time, we will see that Eq. (4) results in novel properties, absent for the planar case. The important difference in our work [Eq. (4)] from the standard skyrmion equation is the presence of the spatial dependence of the anisotropy and DMI parameters. Note that the tuning of the magnetic parameters (the spatial dependence of magnetocrystalline anisotropy and the Dzyaloshinskii-Moriya coefficient) was proposed very recently in Ref. [39] as a way to build traps for skyrmions in flat magnets.

The key finding of the current study is the presence of an external driving force. The forced skyrmion equation was not considered previously. A spatially dependent external force $f(\rho)$ results in the absence of a strictly normal magnetization pattern. More importantly, as we will see below, it provides an alternative mechanism for skyrmion stabilization, which results in tunable-size skyrmions.

The boundary condition for Eq. (4) at the origin is $\Theta(0) = 0$. The value of $\Theta(\infty) = Q\pi$ gives a winding number of the magnetization through directions $\mathbf{n}$ and $-\mathbf{n}$ (skyrmion chirality) as $Q = \pm 1$. The case of $Q = 0$ can be either a skyrmionium state ($Q = 0$) [29,30] or a topologically trivial state. Four solutions of Eq. (4) with different Q are shown in Figs. 1(c) and 1(d) and are discussed below. While $\mathscr{D}_2 \propto 1/r$ and can be considered as a small parameter for wide indentations, the key role in the stabilization of solutions is played by the force $f(\rho)$ depending on $\mathscr{D}_1' \propto \varkappa_1'$, which in turn depends only on the shape of the indentation edge and is not influenced by its radius.

B. Skyrmion pinning in nanoindentation

Based on the forced skyrmion equation, Eq. (4), we obtain two distinct ways to control the type of magnetic texture: (i) the geometry-induced DMI in the left-hand side of Eq. (4a), resulting in the stabilization of small-radius skyrmions [27], and (ii) the effective external driving force originating from the inhomogeneity of the local curvature [Eq. (4b)]. In the following, we show that the latter case allows for the formation of chiral skyrmions of tunable radii.

For a nanoindentation geometry, Fig. 1(a), the ground state of the system is a quasinormal magnetization distribution indicated with a blue solid line in Fig. 1(c). The deviation of the local magnetization from the strictly normal direction is an exchange-driven effect, forcing the magnetization distribution to be homogeneous in the laboratory reference frame. For a slowly varying curvature $\varkappa_1$ (i.e., $|\varkappa_1'| \ll 1$) and large indentation radius $R_{1,2} \gg 1$, one can omit the terms inversely proportional to powers of $R_{1,2}$ in Eq. (4a) and obtains $\Theta(\rho) \approx -\varkappa_1' r/\rho$. Other possible solutions represent Néel skyrmions and a skyrmionium.

While small-radius skyrmions can appear for an arbitrary geometry-induced DMI with the radius governed by the DMI coefficient [27,28], in the present case, we obtain three magnetization textures with different winding numbers Q [Fig. 1(c)]. Inner and outer bends with positive and negative signs of $\mathscr{D}_1$, respectively, support skyrmions with $Q = \pm 1$ and a skyrmionium state with $Q = 0$.

Analytically, we consider a model with a sharp bell-shaped bend of half width $w \ll 1$ and curvature amplitude $\varkappa_0$; see Appendix C for details. Then, the curvature can be represented as

$$\varkappa_1(\rho) = \alpha\left[\delta(\rho - R_1) - \delta(\rho - R_2)\right], \tag{5}$$

with $\delta(\bullet)$ being the Dirac δ function and $\alpha > 0$ being the bending angle. Both radii of the indentation are assumed to be large, $R_2 > R_1 \gg 1$. The curvature [Eq. (5)] describes a nanoindentation in a flat film with a flat inner part and a right-cone lateral face. It allows us to simplify the total energy [Eq. (3)] and skyrmion equation [Eq. (4)] with $\mathscr{D}_2 = 0$ and $\mathscr{K} = 1$.

A large-radius skyrmion profile can be described by a circular domain-wall ansatz

$$\Theta_{\rm sk} = 2\arctan\left[p\exp(\rho - R_{\rm sk})\right] + (p-1)\pi/2, \tag{6}$$

with $p = \pm 1$ for outward and inward magnetization rotation, respectively, and $R_{\rm sk}$ being its radius. Then the total energy reads

$$\mathcal{E}[\Theta_{\rm sk}] = \int \mathscr{E}\rho\, d\rho = 4R_{\rm sk} - 2p\alpha\Big[R_1\,\mathrm{sech}(R_{\rm sk} - R_1) - R_2\,\mathrm{sech}(R_{\rm sk} - R_2)\Big]. \tag{7}$$

Here, the first and second terms represent the energy of a circular domain wall of radius $R_{\rm sk}$ and the contribution of the effective DMI, respectively, compared with Eq. (5) [40]. If the domain wall is localized near R_1 and R_2, the stability conditions read

$$p\alpha > \frac{4}{R_1} \quad \text{for the inner bend, and} \tag{8a}$$

$$-p\alpha > \frac{4}{R_2} \quad \text{for the outer bend.} \tag{8b}$$

See Appendix C for details. Because of the different sign of the effective DMI in the inner and outer bends, skyrmions of different chiralities can be pinned. This is also the reason for the stabilization of a skyrmionium state with zero total winding; see the orange dashed line in Fig. 1(c). A wider skyrmion can be pinned at the first bend with a smaller bending angle α.

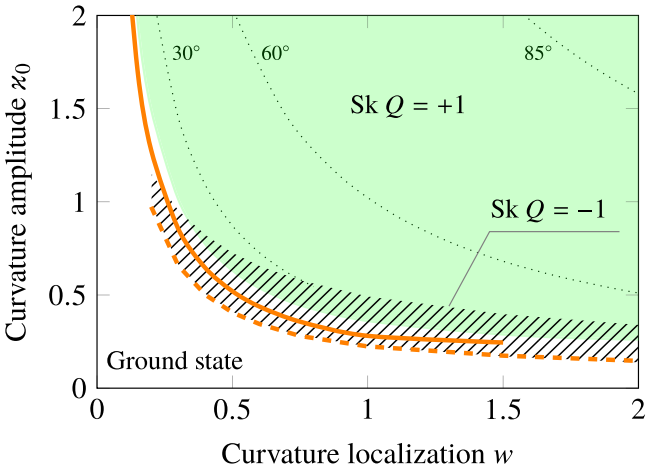

FIG. 2. Stability regions of skyrmions in terms of the curvature amplitude $\varkappa_0$ and curvature spatial localization w. The skyrmion with $Q = +1$ pinned at the inner bend of the nanoindentation with $R_i = 10$ and $R_o = 50$ is stable in the green-shaded region. The orange line shows the corresponding asymptotics for a sharp bend Eq. (8a) and three dotted curves are isolines for α of 30°, 60°, and 85° [bend inclination angle, Fig. 1(a)]. The skyrmion with $Q = -1$ pinned at the outer bend of the nanomembrane with $R_i = 10$ and $R_o = 15$ is stable in the dashed region. The asymptotics from Eq. (8b) is shown by the dashed line.

C. Numerical study of skyrmion stability

To model the curvature of a finite spatial localization, we choose the first principal curvature as a sum of two bell-shaped functions with the maximal value $\varkappa_0$ strongly localized in rings of radii $(R_i - w, R_i + w)$ and $(R_o - w, R_o + w)$. The curvature is zero outside these rings; see Appendix C for details.

Figure 1(c) shows four solutions of Eq. (4a) for a concave nanoindentation [Fig. 1(a)]: the ground state (blue dashed line), two skyrmions with different signs of Q (solid red and green lines), and the skyrmionium state (orange dashed line). A magnetic domain wall is pinned near the maximum of the curvature and slightly shifted toward the bottom flat side of the sample. The impact of a finite curvature is shown in Fig. 2 using the stability analysis described in Sec. IV of [40]: we study the eigenmodes of linear excitations on the skyrmion background. In all cases, radial instability determines the different region boundaries shown in Fig. 2.

There are separate stability regions for skyrmions of different winding numbers Q. Skyrmions with $Q = +1$ pinned at the inner bend of the indentation are stable in a wide range of curvature amplitude $\varkappa_0$ and half-width w; see the green-shaded area in Fig. 2. Skyrmions with $Q = -1$ are stable in a narrow dashed-shaded area. The upper boundary of the stability region is related to the small enough distance between the inner and outer bends.

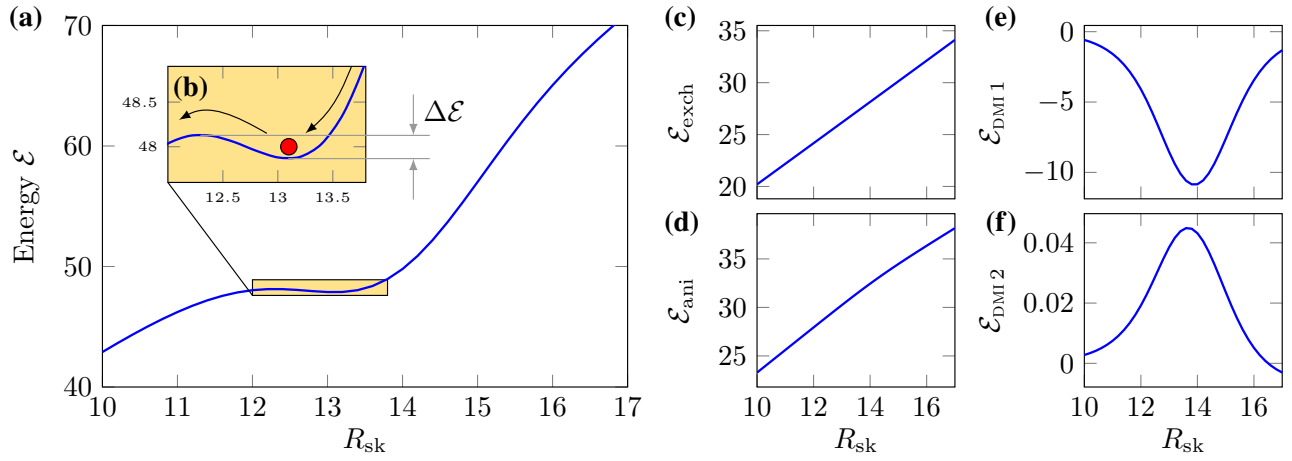

FIG. 3. Pinning of a skyrmion on the inner bend. (a) Total energy of a skyrmion as a function of its radius $R_{\rm sk}$ for $w = 1.5$ and $\varkappa_0 = 0.25$ with $R_i = 15$ (bending angle $\alpha = 26^\circ$). The energy profile has a minimum near $R_1(R_i) = 13.9$. (b) Magnified region of the local minimum in $\mathcal{E}$. Pinning is schematically shown with a red point moving from the right top corner and stopped in the local energy minimum. (c)–(f) Energy profiles of exchange, effective anisotropy, and two effective DMI; see the energy density in Eq. (3). Only the energy related with $\mathscr{D}_1$ in (d) allows pinning, while $\mathcal{E}_{\rm DMI\,2}$ is two orders smaller in magnitude for any finite $\mathscr{D}_2 \neq 0$.

An increase of the curvature influences the domain-wall shape. When a critical value of $\varkappa_0$ is reached, the domain wall slides down, completing the magnetization reversal to the ground state. The analytically predicted lower boundaries of the stability regions for the pinning in the inner and outer bends [Eq. (8)] closely coincide with the numerically calculated ones in a wide range of parameters; see the solid and dashed orange lines in Fig. 2. The different stability regions for skyrmions with $Q = \pm 1$ are related to the effective DMI in the inner and outer bends of the nanoindentation: the sign of $\mathscr{D}_1$ selects the clockwise or counterclockwise direction of magnetization winding.

Using the ansatz in Eq. (6) with $p = 1$, we estimate the energy profile [Eq. (3)] and energy gap, allowing a skyrmion to be pinned at a bend; see Fig. 3. We note that the ansatz in Eq. (6) does not take into account any specific characteristics of the systems and might underestimate the pinning strength. The total energy shown in Fig. 3(a) is a sum of four terms, shown in Figs. 3(c)–3(f). Exchange and anisotropy energies (related to the coefficient $\mathscr{K}$) are monotonically increasing functions and cannot pin the skyrmion. The energy $\mathcal{E}_{\rm DMI\,2}$, related to $\mathscr{D}_2$, shows a small maximum, which does not contribute significantly to the pinning effect. In contrast, the energy $\mathcal{E}_{\rm DMI\,1}$, related to $\mathscr{D}_1 \propto \varkappa_1$, exhibits a pronounced minimum near R_1, resulting in the appearance of a local minimum in the total energy.

We estimate the energy gap of $\Delta\mathcal{E} = 750$ K for the case of a nanoindentation of Co/Pt stacks ($A = 10$ pJ/m, $K_u = 0.3$ MJ/m^3, $M_S = 480$ kA/m, and thickness of the Co layer $h = 0.6$ nm) with a geometry considered in Fig. 3.

III. DISCUSSION

The geometry of a ferromagnetic film makes a significant impact on static and dynamic skyrmion properties. Finite dimensions of nanostructures can lead to the confinement of a skyrmion [38] and skyrmion formation under an external influence [41]. Considering curvilinear effects, an alternative way to stabilize skyrmions is to utilize a curvature-induced DMI of interfacial type in samples with a geometrically defined axis of anisotropy [25–28].

In this work, we studied magnetic nanoindentations of radial symmetry with a locally perpendicular easy axis of magnetization. We proposed a coordinate transformation allowing us to incorporate the metric of the curved surface into spatially dependent material parameters and obtain a driven skyrmion equation with the left-hand side in the form of a well-known description of flat systems; see, e.g., [36]. Our approach allowed us to directly compare effects of curvature with well-known flat films with intrinsic chiral interactions and uncovers two mechanisms of skyrmion stabilization.

(i) The first mechanism is based on the appearance of the geometry-induced Dzyaloshinskii-Moriya interaction [27]. The consequence of this effect is the possibility to form small-sized skyrmions in the region of maximal curvature.

(ii) The second mechanism, addressed in this work, governs the skyrmion size by the curvature gradient, which results in tunable-size skyrmions.

In both of these cases, skyrmions are static solutions because their structure is determined by the distribution of material parameters. The size of the skyrmions of type (i) is limited by the characteristic magnetic length ℓ due to their

localization in the region of the curvature maximum, where the curvature is approximately constant [27]. The spatial inhomogeneity of the DMI and anisotropy coefficients becomes crucial when considering the magnetization textures of type (ii).

In contrast to skyrmions, stabilized by the intrinsic DMI, the topologically nontrivial structures, discussed in the current work, are not mobile. However, it is a way to create individual skyrmions and skyrmioniums as well as their artificial lattices at room temperature, which is important from a fundamental point of view and for applications in spintronic devices, e.g., for enhancing the topological Hall effect [42–48].

In the case of one-dimensional systems, the local change in the anisotropy is the source of a domain-wall nucleation [49] and attractive or repulsive pinning in a magnet [50]. The stabilization of circular domain walls usually appears due to magnetostatics, while the size can also be governed by the inhomogeneity of the anisotropy [6,8,51]. In a curvilinear nanomembrane, two effective anisotropies and two effective DMI appear and each of them is related to the corresponding principal curvature [25,26]. For the radially symmetric textures considered in this work, one of the curvature-induced anisotropies disappears due to the symmetry of the object and texture, while the sum of the intrinsic anisotropy and the second geometry-induced one is incorporated in the coefficient $\mathscr{K}$ in Eq. (4a); see the expression in Eq. (B14a).

The simplest way to create and annihilate a skyrmion in the nanoindentation is via a pulse of perpendicular spin-polarized current or magnetic field along the $\hat{\mathbf{z}}$ axis. An incomplete hysteresis loop from the initially saturated state along $-\hat{\mathbf{z}}$ shows different switching fields for the planar parts and lateral sides of the indentation, which results in the appearance of domain walls in the indentation edges [52]. While the coordinate-dependent anisotropy only changes the slope of the energy landscape [Fig. 3(d)], the first DMI coefficient $\mathscr{D}_1$ depends only on the bend parameters [see Eq. (B14b)] and reduces the Néel domain-wall energy of the preferred chirality during the domain-wall positioning on the bend. The second DMI coefficient $\mathscr{D}_2$ [see (B14b)] can also lower the domain-wall energy, but it is inversely proportional to the radius of the nanoindentation and does not significantly affect the magnetization texture (in the case of large objects). Note that the crucial role is played by a spatially localized distribution of $\mathscr{D}_1$ only, whose gradient results in a local energy minimum for a skyrmion with respect to its radius; see Fig. 3.

The skyrmion radius is determined by the relation of the DMI coefficient to the domain-wall energy density in flat systems. Therefore, large-radius skyrmions can be described by a circular domain-wall ansatz [38,40]. In contrast to this case, a bend of a ferromagnetic nanomembrane provides a pinning potential for a circular domain wall separating flat and inclined parts. Then, the size of a chiral texture is determined both by the area enclosed by a bend and the effective DMI exceeding the given critical value. This is similar to the appearance of one-dimensional chiral domain walls whose energy decreases proportionally to the DMI coefficient [38,53].

Using a model of a circular curved nanomembrane projected to a plane [Eq. (2)], we demonstrated a good agreement with the exact numerical calculations for the bend of a finite width; see Fig. 2 and Appendix C for details. Our analytical model takes into account only the first curvature-induced DMI $\mathscr{D}_1$ in the form of a Dirac δ function, neglecting the second DMI coefficient, $\mathscr{D}_2$, and with the constant anisotropy $\mathscr{K}_0 = 1$. The coordinate-dependent coefficient $\mathscr{D}_1$ determines the skyrmion radius R_{sk}. Note that, in this case, the skyrmion equation [Eq. (4a)] differs from the planar case only by the presence of a driving force [Eq. (4b)] appearing after the energy variation. Therefore, this allows us to predict the same properties of circular Néel domain walls in planar films with nonzero DMI in a narrow circular region: Néel domain walls should be pinned in the region with the DMI sign selecting the magnetization rotation direction inward or outward.

The estimation of the pinning strength for a skyrmion formed in a Co/Pt-based nanoindentation with $\varkappa_0 = 0.25$ and $w = 1.5$ (bending angle $\alpha \approx 26^\circ$ with the bend width of about 15 nm) shown in Fig. 3 leads to the energy gap of about 10^3 K, stabilizing the skyrmion on a bend. This model refers to actively studied nanopatterned media, including circular nanoindentations [54–57] and convex structures such as cones [58,59], caps [60–62], and spheres [27]. One can compare this prediction with the experiments for caps and nanoindentations [52,54,56,57] covered with perpendicularly magnetized Co/Pt multilayers. The presence of experimentally observed single-domain features localized in curved regions is typically attributed to a (partial) exchange decoupling between the magnetic nanostructure and a flat film. Here, we show how the tilt of the anisotropy axis on a bend of a nanomembrane can provide a significant contribution to the domain-wall pinning due to the geometry-induced effective DMI, which is strongly localized in the bend area; see Fig. 3. Note that an imperfect circular shape of indentation edges, e.g., elliptical deformation, will change the boundaries of skyrmion stability regions and the instability symmetry, but does not change our conclusions. We speculate that these objects can be the large-size skyrmions discussed in this work.

ACKNOWLEDGMENTS

The authors thank A. N. Bogdanov (IFW Dresden) for fruitful discussions. O.V.P. and D.D.S. thank Helmholtz-Zentrum Dresden-Rossendorf e. V. (HZDR), where part of this work was performed, for their kind hospitality, and acknowledge the support from the Alexander von Humboldt Foundation (Research Group Linkage Programme).

V.P.K. acknowledges the support from the Alexander von Humboldt Foundation. O.V.P. acknowledges the support from DAAD (Grant No. 91530902). This work was financed in part via the BMBF project GUC-LSE (federal research funding of Germany FKZ: 01DK17007); the German Research Foundation (DFG) Grant No. MA 5144/9-1; and the National Academy of Sciences of Ukraine, Project No. 0116U003192. A.S. is supported by the U.S. Department of Energy.

APPENDIX A: SURFACES OF REVOLUTION

We form the surface ς by the revolution of a curve $\boldsymbol{\gamma} = r\hat{\mathbf{r}} + z\hat{\mathbf{z}}$ around $\hat{\mathbf{z}}$: $\varsigma(r,\chi) = \{r\cos\chi, r\sin\chi, z(r)\}$. Here and below, all distances are measured in the units of the magnetic length ℓ. The complete definition of geometrical properties of ς can be inferred through two principal curvatures,

$$\varkappa_1(r) = \frac{\partial_{rr}^2 z}{Z^3}, \quad \varkappa_2(r) = \frac{\partial_r z}{rZ}, \tag{A1}$$

with $Z(r) = \sqrt{1+(\partial_r z)^2}$. Note that the first principal curvature coincides with the curvature of the generatrix $\boldsymbol{\gamma}$. In the case of a surface of revolution, there is a relation $\varkappa_1 = \partial_r(r\varkappa_2)$. The way to extend ς along the normal $\mathbf{n}$ without any self-intersection in the surface vicinity is to introduce coordinates along the principal directions (radial and polar directions), $\mathbf{e}_1 = \partial_r\varsigma/|\partial_r\boldsymbol{\gamma}|$ and $\mathbf{e}_2 = \{-\sin\chi, \cos\chi, 0\}$. Then the normal is given by $\mathbf{n} = \mathbf{e}_1 \times \mathbf{e}_2$ and the area element is $dS = rZ\,dr\,d\chi$.

APPENDIX B: ENERGY OF A CURVILINEAR FERROMAGNETIC NANOMEMBRANE

The energy of a ferromagnetic nanomembrane reads

$$E = h\int\left[A\mathscr{E}_{\rm ex} - K_u m_n{}^2 - \frac{M_S}{2}(\mathbf{m}\cdot\mathbf{H}_d)\right]dS, \tag{1'}$$

where A is the exchange stiffness, $K_u > 0$ is the constant of uniaxial anisotropy, m_n is the normal magnetization component, and $\mathbf{H}_d$ is the demagnetizing field. In the thin-film limit $h \lesssim \ell$, we incorporate the magnetostatic effects in the effective anisotropy $K = K_u - 2\pi M_S^2$ [31–34].

It is natural to use a curvilinear reference frame, generated by the surface ς for the description of the magnetization pattern. This approach recovers the translational symmetry of anisotropy for films with a uniaxial, easy-normal anisotropy [Eq. (1′)] [25,26]. The exchange energy density for an angular parametrization of the magnetization texture $\mathbf{m} = \sin\theta\cos\phi\mathbf{e}_1 + \sin\theta\sin\phi\mathbf{e}_2 + \cos\theta\mathbf{n}$ reads [25,26]

$$\mathscr{E}_{\rm ex} = [\nabla\theta - \boldsymbol{\Gamma}]^2 + \left[\sin\theta\,(\nabla\phi - \boldsymbol{\Omega}) - \cos\theta\,\partial_\phi\boldsymbol{\Gamma}\right]^2, \tag{B1}$$

with $\boldsymbol{\Omega}$ being a spin connection with components $\Omega_\mu = \mathbf{e}_1\cdot\nabla_\mu\mathbf{e}_2$ for $\mu = 1,2$ and the vector $\boldsymbol{\Gamma}(\phi) = \varkappa_1\cos\phi\mathbf{e}_1 + \varkappa_2\sin\phi\mathbf{e}_2$. Here, $\nabla = (\mathbf{e}_1/Z)\partial_r + (\mathbf{e}_2/r)\partial_\chi$ denotes a surface "del" operator in its curvilinear form. In particular, for surfaces of revolution, $\Omega_1 = 0$ and $\Omega := \Omega_2 = -1/(rZ)$.

The static Landau-Lifshitz equations have the following form:

$$\nabla^2\theta - \sin\theta\cos\theta\left[1 - \left(\partial_\phi\boldsymbol{\Gamma}\right)^2 + (\nabla\phi - \boldsymbol{\Omega})^2\right] + \cos 2\theta\,(\nabla\phi - \boldsymbol{\Omega})\cdot\partial_\phi\boldsymbol{\Gamma} - \nabla\cdot\boldsymbol{\Gamma} = 0, \tag{B2a}$$

$$\nabla\cdot\left(\sin^2\theta\nabla\phi\right) + \sin^2\theta\left[(2\nabla\theta - \boldsymbol{\Gamma})\cdot\partial_\phi\boldsymbol{\Gamma} - \nabla\cdot\boldsymbol{\Omega}\right] - \sin\theta\cos\theta\left[2\nabla\theta\cdot\boldsymbol{\Omega} + \nabla\cdot\partial_\phi\boldsymbol{\Gamma} + (\nabla\phi - \boldsymbol{\Omega})\cdot\boldsymbol{\Gamma}\right] = 0. \tag{B2b}$$

There exists a class of azimuthally symmetric solutions

$$\theta = \theta(r), \quad \phi = 0,\pi, \quad \cos\phi = \pm 1. \tag{B3}$$

For this class of solutions, it is convenient to use another angular parametrization,

$$\mathbf{m} = \sin\Theta(r)\mathbf{e}_1 + \cos\Theta(r)\mathbf{n}, \quad \Theta\in\mathbb{R}, \tag{B4}$$

to reduce the number of independent variables. Then the energy density [Eq. (B1)] reads

$$\mathscr{E}_{\rm ex} = \frac{(\partial_r\Theta)^2}{Z^2} - \frac{2\varkappa_1\partial_r\Theta}{Z} + \varkappa_1^2 + \varkappa_2^2 + (\Omega^2 - \varkappa_2^2)\sin^2\Theta + 2\Omega\varkappa_2\sin\Theta\cos\Theta. \tag{B5}$$

Now, we want to find a transformation of variables that incorporates the effects of curvature in Eq. (B5) and reduces its analytical form to a standard expression of the exchange energy of the flat magnet in the polar reference frame. We start with the case of an isotropic magnet, $K = 0$. The ground state of the model is the homogeneous (in the physical space) state. We limit ourselves to the homogeneous magnetization distributions along the z axis with $\mathbf{m}_h = \mathcal{C}_h\hat{\mathbf{z}}$:

$$\cos\Theta_h = \frac{\mathcal{C}_h}{Z}, \quad \sin\Theta_h = \frac{\mathcal{C}_h\partial_r z}{Z}, \tag{B6}$$

with $\mathcal{C}_h = \pm 1$.

It is instructive to represent the energy functional in Eq. (B5) in terms of the angle ψ, which characterizes the deviation from the homogeneous state

$$\Theta(r) = \Theta_h(r) + \psi(r). \tag{B7}$$

The exchange energy density in the ψ notation has a simple form:

$$\mathscr{E}_{\rm ex} = \frac{(\partial_r\psi)^2}{Z^2} + \frac{\sin^2\psi}{r^2}. \tag{B8}$$

By minimizing this energy, one gets the static equations

$$\frac{r}{Z}\frac{d}{dr}\left(\frac{r}{Z}\frac{d\psi}{dr}\right) - \sin\psi\cos\psi = 0. \tag{B9}$$

Let us map the revolution surface to the plane by introducing the surface polar coordinate $\rho = \rho(r)$ as follows:

$$\rho(r) = r\exp\int_r^\infty \left[1 - \sqrt{1 + \left(\frac{dz}{d\zeta}\right)^2}\right]\frac{d\zeta}{\zeta}. \tag{2′}$$

Such a transformation allows us to rewrite Eq. (B9) in the form

$$\psi'' + \frac{1}{\rho}\psi' - \frac{1}{\rho^2}\sin\psi\cos\psi = 0, \tag{B10}$$

which is well known [63] to describe radially symmetric magnetic textures for an isotropic planar ferromagnet. Figure 4(a) shows the relation between the surface polar coordinate ρ and the distance to the symmetry axis r. The dependence $\rho(r)$ has the limiting values $\rho(0) = 0$ and $\rho(\infty) = \infty$; far from the center of the nanoindentation, $\rho(r) = r$.

We look for a skyrmion solution of Eq. (B9), which satisfies the boundary conditions

$$\begin{aligned}\psi(r=0) &= \psi(\rho=0) = \pi,\\ \psi(r=\infty) &= \psi(\rho=\infty) = 0.\end{aligned} \tag{B11}$$

The corresponding solution of Eq. (B10) is the well-known Belavin-Polyakov skyrmion solution [64]

$$\begin{aligned}\tan\frac{\psi_{\rm BP}}{2} &= \frac{R}{\rho}, \quad R = \text{const},\\ \Theta_{\rm BP}(\rho) &= \Theta_h(\rho) + \psi_{\rm BP}(\rho).\end{aligned} \tag{B12}$$

The energy of the Belavin-Polyakov skyrmion $E = 8\pi Ah$ does not depend on its radius, which results in the skyrmion instability. An efficient way for the static stabilization of the skyrmion structure is to take into account both the anisotropy and DMI. In our case, both interactions appear effectively due to the curvature of the nanomembrane and they are coordinate dependent.

The energy [Eq. (1′)] for the radially symmetric solution [Eq. (B4)] up to a constant reads

$$\mathcal{E} = \frac{E}{2\pi Ah} = \int \mathscr{E}\,\rho\,d\rho, \tag{B13}$$

with the energy density

$$\mathscr{E} = \underbrace{\Theta'^2 + \frac{\sin^2\Theta}{\rho^2}}_{\text{exchange}} + \underbrace{\mathscr{K}\sin^2\Theta}_{\text{anisotropy}} - \underbrace{\mathscr{D}_1\Theta'}_{\text{DMI 1}} - \underbrace{\mathscr{D}_2\frac{\sin\Theta\cos\Theta}{\rho}}_{\text{DMI 2}}, \tag{3′}$$

where coefficients are functions of the principal curvatures of the nanomembrane $\varkappa_1(\rho)$ and $\varkappa_2(\rho)$. The parameter $\mathscr{K}$ characterizes the geometrically induced, exchange-driven anisotropy

$$\mathscr{K} = \frac{r^2}{\rho^2}\left(1 - 2\varkappa_2^2\right), \tag{B14a}$$

with $r = r(\rho)$ here and below. Parameters $\mathscr{D}_1$ and $\mathscr{D}_2$ can be treated as parameters of the geometrically induced, exchange-driven DMI:

$$\mathscr{D}_1 = \frac{2r\varkappa_1}{\rho}, \quad \mathscr{D}_2 = 2r'\varkappa_2. \tag{B14b}$$

There is a striking correspondence between the energy density of the nanoindentation [Eq. (3′)] and the energy density of a chiral skyrmion in a planar magnet with an intrinsic DMI [36]. Nevertheless, it is important to stress that all these effective interactions are characterized by the spatially dependent parameters, $\mathscr{K}(\rho)$, $\mathscr{D}_1(\rho)$, and $\mathscr{D}_2(\rho)$. The typical spatial distribution of these parameters is shown in Fig. 5. The first DMI coefficient $\mathscr{D}_1 \propto \varkappa_1(\rho)$. The second DMI coefficient $\mathscr{D}_2 \propto \varkappa_2$ is nonzero only in the tilted part of the nanoindentation.

APPENDIX C: MODEL OF A NANOINDENTATION

We model a nanoindentation with a flat inner part considering a sharp indent of a conic frustum shape in the flat film

$$z_{\rm sh}(r) = \begin{cases} 0, & \text{when } r < R_i,\\ (r - R_i)\tan\alpha, & \text{when } R_i \le r \le R_o,\\ z_0, & \text{when } r > R_o,\end{cases} \tag{C1}$$

with $\tan\alpha = z_0/(R_o - R_i)$. Now we project this conic frustum to the surface, using the mapping from Eq. (2′)

$$r(\rho) = \begin{cases} \dfrac{R_i}{R_1}\rho, & \text{when } \rho < R_1,\\ R_2\left(\dfrac{\rho}{R_2}\right)^{\cos\alpha}, & \text{when } R_1 < \rho < R_2,\\ \rho, & \text{when } \rho > R_2,\end{cases} \tag{C2}$$

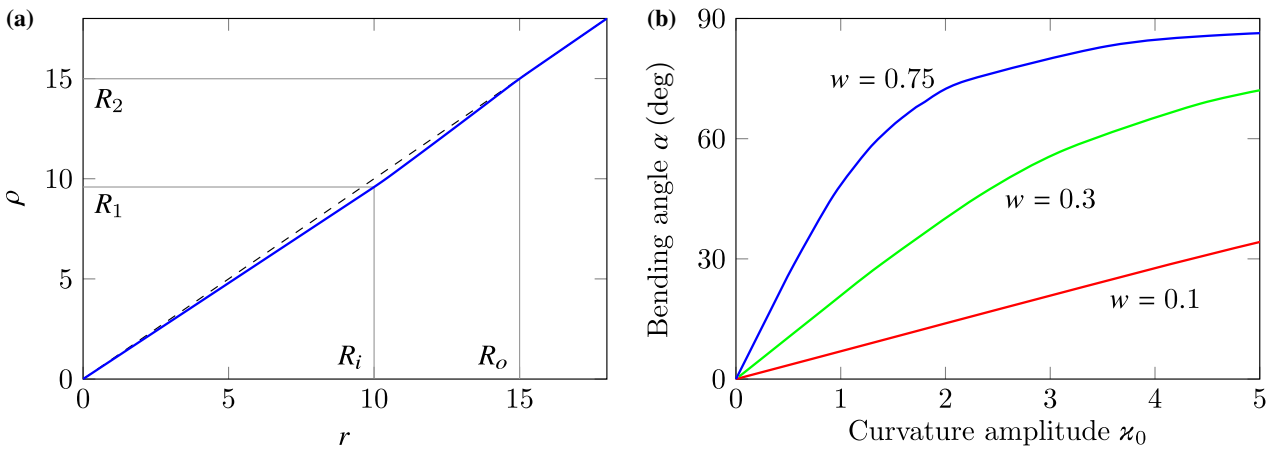

FIG. 4. Characteristics of the nanomembrane geometry. (a) A relation between the distance to the axis r of the sample and the surface polar coordinate ρ according to Eq. (2). The dependence $\rho(r)$ is shown with a line and we bisect the quadrant with a dashed line. The plot is built for parameters taken from Fig. 1. Here, $R_1 \approx 9.59$ and $R_2 \approx 14.99$. (b) The bending angle α for different spatial localizations w of the curvature.

with $R_1 = R_o(R_i/R_o)^{\sec\alpha} < R_2$ and $R_2 = R_o$. Then the principal curvatures of the nanomembrane are given by

$$\varkappa_1(\rho) = \alpha\,[\delta(\rho - R_1) - \delta(\rho - R_2)]\,, \qquad (5')$$

$$\varkappa_2(\rho) = \begin{cases} 0, & \text{when } \rho < R_1 \text{and } \rho > R_2, \\ \dfrac{\alpha\cos\alpha}{R_2}\left(\dfrac{R_2}{\rho}\right)^{\cos\alpha}, & \text{when } R_1 < \rho < R_2, \\ \dfrac{\alpha\cos(\alpha/2)}{2R_1}, & \text{when } \rho = R_1, \\ \dfrac{\alpha\cos(\alpha/2)}{2R_2}, & \text{when } \rho = R_2, \end{cases} \qquad (C3)$$

with $\delta(\bullet)$ being the Dirac δ function.

We assume that both R_1 and R_2 are large enough to omit all terms of the order $1/\rho$ and higher in the energy density [Eq. (3′)]. Then, the expression in Eq. (3′) can be written as

$$\mathscr{E}_0 = \Theta'^2 + \mathscr{K}_0 \sin^2\Theta - 2\alpha\frac{r}{\rho}\left[\frac{R_1}{R_i}\delta(\rho - R_1) - \delta(\rho - R_2)\right]\Theta', \qquad (C4)$$

where

$$\mathscr{K}_0 = \begin{cases} \left(\dfrac{R_2}{R_i}\right)^{2(\sec\alpha - 1)}, & \text{when } \rho < R_1, \\ \left(\dfrac{R_2}{\rho}\right)^{2(1-\cos\alpha)}, & \text{when } R_1 \le \rho \le R_2, \\ 1, & \text{when } \rho > R_2. \end{cases} \qquad (C5)$$

This expression can be simplified to $\mathscr{K}_0 \approx 1$ in a wide range of ratios R_1/R_2 for small angles α and in a wide range of α if inner and outer radii R_1 and R_2 are comparable; see Fig. 5.

Applying here the circular domain-wall ansatz [Eq. (6)], we obtain the total energy [Eq. (7)]. The condition for the existence of a local minimum in Eq. (7) gives the expressions in Eq. (8).

Now, to take into account the finite localization region of the curvature, we smooth the shape [Eq. (C1)] using the convolution of the sharp conic frustum $z_{\rm sh}(r)$ with the mollifier $g_w(r)$,

$$g_w(\zeta) = \begin{cases} \dfrac{C_g}{w}\exp\left(\dfrac{w^2}{\zeta^2 - w^2}\right), & \text{when } -w \le \zeta \le w, \\ 0, & \text{otherwise}, \end{cases} \qquad (C6)$$

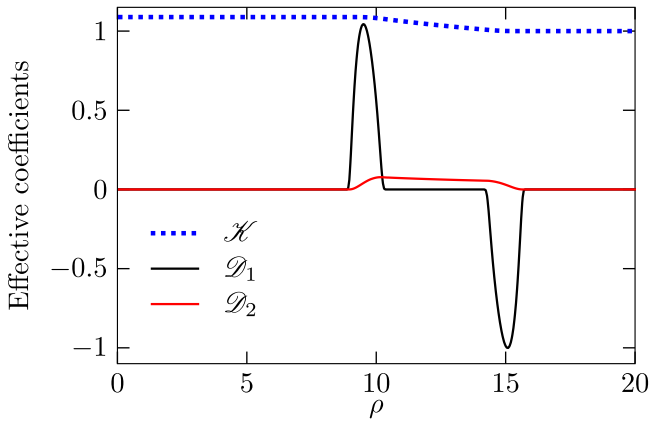

FIG. 5. Effective coefficients of the energy of the radially symmetric solution. Effective anisotropy [Eq. (B14a)] and the two DMI coefficients [Eq. (B14b)] as a function of the ρ coordinate for the sample parameters are shown in Fig. 1.

in the following way:

$$z(r) = \int_{-w}^{\min\{r,w\}} g_w(\zeta) z_{\rm sh}(r-\zeta)\, d\zeta . \qquad \text{(C7)}$$

Here, $C_g \approx 2.25$ from the condition $\int_{-w}^{w} g_w(\zeta)\, d\zeta = 1$. Mollifying Eq. (C7) guarantees that the first principal curvature $\varkappa_1(r)$ is nonzero only in a region of $2w$ around the bend. The bending angle as a function of w and curvature amplitude $\varkappa_0$ is shown in Fig. 4(b). All lines asymptotically tend to $\alpha = 90^\circ$.

[1] Naoto Nagaosa and Yoshinori Tokura, Topological properties and dynamics of magnetic skyrmions, Nat. Nanotechnol. **8**, 899 (2013).

[2] Giovanni Finocchio, Felix Büttner, Riccardo Tomasello, Mario Carpentieri, and Mathias Kläui, Magnetic skyrmions: From fundamental to applications, J. Phys. D Appl. Phys. **49**, 423001 (2016).

[3] Roland Wiesendanger, Nanoscale magnetic skyrmions in metallic films and multilayers: A new twist for spintronics, Nat. Rev. Mater. **1**, 16044 (2016).

[4] Albert Fert, Nicolas Reyren, and Vincent Cros, Magnetic skyrmions: Advances in physics and potential applications, Nat. Rev. Mater. **2**, 17031 (2017).

[5] Jan Seidel, ed., *Topological Structures in Ferroic Materials* (Springer International Publishing, Switzerland, 2016).

[6] M. V. Sapozhnikov, S. N. Vdovichev, O. L. Ermolaeva, N. S. Gusev, A. A. Fraerman, S. A. Gusev, and Yu. V. Petrov, Artificial dense lattice of magnetic bubbles, Appl. Phys. Lett. **109**, 042406 (2016).

[7] M. V. Sapozhnikov and O. L. Ermolaeva, Two-dimensional skyrmion lattice in a nanopatterned magnetic film, Phys. Rev. B **91**, 024418 (2015).

[8] M. V. Sapozhnikov, Skyrmion lattice in a magnetic film with spatially modulated material parameters, J. Magn. Magn. Mater. **396**, 338 (2015).

[9] J. C. Gallagher, K. Y. Meng, J. T. Brangham, H. L. Wang, B. D. Esser, D. W. McComb, and F. Y. Yang, Robust Zero-field Skyrmion Formation in FeGe Epitaxial Thin Films, Phys. Rev. Lett. **118**, 027201 (2017).

[10] Kai Litzius, Ivan Lemesh, Benjamin Krüger, Pedram Bassirian, Lucas Caretta, Kornel Richter, Felix Büttner, Koji Sato, Oleg A. Tretiakov, Johannes Förster, Robert M. Reeve, Markus Weigand, Iuliia Bykova, Hermann Stoll, Gisela Schütz Geoffrey S. D. Beach, and Kläui Mathias, Skyrmion Hall effect revealed by direct time-resolved X-ray microscopy, Nature Physics **13**, 170 (2016).

[11] Jan Müller, Magnetic skyrmions on a two-lane racetrack, New J. Phys. **19**, 025002 (2017).

[12] Andrea De Lucia, Kai Litzius, Benjamin Krüger, Oleg A. Tretiakov, and Mathias Kläui, Multiscale simulations of topological transformations in magnetic-skyrmion spin structures, Phys. Rev. B **96**, 020405 (2017).

[13] Christina Psaroudaki and Daniel Loss, Skyrmions Driven by Intrinsic Magnons, Phys. Rev. Lett. **120**, 237203 (2018).

[14] Riccardo Hertel, Curvature-induced magnetochirality, SPIN **03**, 1340009 (2013).

[15] Arseni Goussev, J. M. Robbins, and Valeriy Slastikov, Domain wall motion in thin ferromagnetic nanotubes: Analytic results, Europhys. Lett. **105**, 67006 (2014).

[16] Arseni Goussev, J. M. Robbins, Valeriy Slastikov, and Oleg A. Tretiakov, Dzyaloshinskii-Moriya domain walls in magnetic nanotubes, Phys. Rev. B **93**, 054418 (2016).

[17] Jorge A. Otálora, Ming Yan, Helmut Schultheiss, Riccardo Hertel, and Attila Kákay, Curvature-induced Asymmetric Spin-wave Dispersion, Phys. Rev. Lett. **117**, 227203 (2016).

[18] Oleg A. Tretiakov, Massimiliano Morini, Sergiy Vasylkevych, and Valeriy Slastikov, Engineering Curvature-induced Anisotropy in Thin Ferromagnetic Films, Phys. Rev. Lett. **119**, 077203 (2017).

[19] P. Landeros and Álvaro S. Núñez, Domain wall motion on magnetic nanotubes, J. Appl. Phys. **108**, 033917 (2010).

[20] J. A. Otálora, J. A. López-López, P. Vargas, and P. Landeros, Chirality switching and propagation control of a vortex domain wall in ferromagnetic nanotubes, Appl. Phys. Lett. **100**, 072407 (2012).

[21] Ming Yan, Christian Andreas, Attila Kákay, Felipe Garcia-Sanchez, and Riccardo Hertel, Chiral symmetry breaking and pair-creation mediated walker breakdown in magnetic nanotubes, Appl. Phys. Lett. **100**, 252401 (2012).

[22] R. Hertel, Ultrafast domain wall dynamics in magnetic nanotubes and nanowires, J. Phys. Condens. Matter **28**, 483002 (2016).

[23] Jorge A. Otálora, Ming Yan, Helmut Schultheiss, Riccardo Hertel, and Attila Kákay, Asymmetric spin-wave dispersion in ferromagnetic nanotubes induced by surface curvature, Phys. Rev. B **95**, 184415 (2017).

[24] J. A. Otálora, A. Kákay, J. Lindner, H. Schultheiss, A. Thomas, J. Fassbender, and K. Nielsch, Frequency line width and decay length of spin waves in curved magnetic membranes, Phys. Rev. B **98**, 014403 (2018).

[25] Yuri Gaididei, Volodymyr P. Kravchuk, and Denis D. Sheka, Curvature Effects in Thin Magnetic Shells, Phys. Rev. Lett. **112**, 257203 (2014).

[26] Denis D. Sheka, Volodymyr P. Kravchuk, and Yuri Gaididei, Curvature effects in statics and dynamics of low dimensional magnets, J. Phys. A: Math. Theor. **48**, 125202 (2015).

[27] Volodymyr P. Kravchuk, Ulrich K. Röler, Oleksii M. Volkov, Denis D. Sheka, Jeroen van den Brink, Denys Makarov, Hagen Fuchs, Hans Fangohr, and Yuri Gaididei, Topologically stable magnetization states on a spherical shell: Curvature-stabilized skyrmions, Phys. Rev. B **94**, 144402 (2016).

[28] Volodymyr P. Kravchuk, Denis D. Sheka, Attila Kákay, Oleksii M. Volkov, Ulrich K. Röler, Jeroen van den Brink, Denys Makarov, and Yuri Gaididei, Multiplet of Skyrmion States on a Curvilinear Defect: Reconfigurable Skyrmion Lattices, Phys. Rev. Lett. **120**, 067201 (2018).

[29] M. Finazzi, M. Savoini, A. R. Khorsand, A. Tsukamoto, A. Itoh, L. Duò, A. Kirilyuk, Th. Rasing, and M. Ezawa, Laser-induced Magnetic Nanostructures with Tunable Topological Properties, Phys. Rev. Lett. **110**, 177205 (2013).

[30] Stavros Komineas and Nikos Papanicolaou, Skyrmion dynamics in chiral ferromagnets, Phys. Rev. B **92**, 064412 (2015).

[31] G. Gioia and R. D. James, Micromagnetics of very thin films, Proc, R. Soc. Lond. A **453**, 213 (1997).

[32] G. Carbou, Thin layers in micromagnetism, Math. Models Methods Appl. Sci. **11**, 1529 (2001).

[33] Robert V. Kohn and Valeriy V. Slastikov, Another thin-film limit of micromagnetics, Arch. Ration. Mech. Anal. **178**, 227 (2005).

[34] Giovanni Di Fratta, Dimension reduction for the micromagnetic energy functional on curved thin films, arXiv:1609.08040v3.

[35] Oleksandr V. Pylypovskyi, Volodymyr P. Kravchuk, Denis D. Sheka, Denys Makarov, Oliver G. Schmidt, and Yuri Gaididei, Coupling of Chiralities in Spin and Physical Spaces: The Möbius Ring as a Case Study, Phys. Rev. Lett. **114**, 197204 (2015).

[36] A. O. Leonov, T. L. Monchesky, N. Romming, A. Kubetzka, A. N. Bogdanov, and R. Wiesendanger, The properties of isolated chiral skyrmions in thin magnetic films, New J. Phys. **18**, 065003 (2016).

[37] A. Bogdanov and A. Hubert, Thermodynamically stable magnetic vortex states in magnetic crystals, J. Magn. Magn. Mater. **138**, 255 (1994).

[38] S. Rohart and A. Thiaville, Skyrmion confinement in ultrathin film nanostructures in the presence of Dzyaloshinskii-Moriya interaction, Phys. Rev. B **88**, 184422 (2013).

[39] D. Toscano, S. A. Leonel, P. Z. Coura, and F. Sato, Building traps for skyrmions by the incorporation of magnetic defects into nanomagnets: Pinning and scattering traps by magnetic properties engineering, arXiv:1810.03754v1.

[40] Volodymyr P. Kravchuk, Denis D. Sheka, Ulrich K. Rößler, Jeroen van den Brink, and Yuri Gaididei, Spin eigenmodes of magnetic skyrmions and the problem of the effective skyrmion mass, Phys. Rev. B **97**, 064403 (2018).

[41] Wanjun Jiang, Wei Zhang, Guoqiang Yu, M. Benjamin Jungfleisch, Pramey Upadhyaya, Hamoud Somaily, John E. Pearson, Yaroslav Tserkovnyak, Kang L. Wang, Olle Heinonen, Suzanne G. E. te Velthuis, and Axel Hoffmann, Mobile Néel skyrmions at room temperature: Status and future, AIP Adv. **6**, 055602 (2016).

[42] U. K. Rößler, A. N. Bogdanov, and C. Pfleiderer, Spontaneous skyrmion ground states in magnetic metals, Nature **442**, 797 (2006).

[43] S. Mühlbauer, B. Binz, F. Jonietz, C. Pfleiderer, A. Rosch, A. Neubauer, R. Georgii, and P. Böni, Skyrmion lattice in a chiral magnet, Science **323**, 915 (2009).

[44] N. Kanazawa, Y. Onose, T. Arima, D. Okuyama, K. Ohoyama, S. Wakimoto, K. Kakurai, S. Ishiwata, and Y. Tokura, Large Topological Hall Effect in a Short-period Helimagnet MnGe, Phys. Rev. Lett. **106**, 156603 (2011).

[45] Dustin A. Gilbert, Brian B. Maranville, Andrew L. Balk, Brian J. Kirby, Peter Fischer, Daniel T. Pierce, John Unguris, Julie A. Borchers, and Kai Liu, Realization of ground-state artificial skyrmion lattices at room temperature, Nat. Commun. **6**, 8462 (2015).

[46] Hiroyuki Fujita and Masahiro Sato, Ultrafast generation of skyrmionic defects with vortex beams: Printing laser profiles on magnets, Phys. Rev. B **95**, 054421 (2017).

[47] Hiroyuki Fujita and Masahiro Sato, Encoding orbital angular momentum of light in magnets, Phys. Rev. B **96**, 060407 (2017).

[48] Shilei Zhang, Florian Kronast, Gerrit van der Laan, and Thorsten Hesjedal, Real-space observation of skyrmionium in a ferromagnet-magnetic topological insulator heterostructure, Nano Lett. **18**, 1057 (2018).

[49] H. Kronmüller, Theory of nucleation fields in inhomogeneous ferromagnets, Phys. Status Solidi (b) **144**, 385 (1987).

[50] R. Skomski, Nanomagnetism, J. Phys. **C15**, R841 (2003).

[51] S. Zhang, A. K. Petford-Long, and C. Phatak, Creation of artificial skyrmions and antiskyrmions by anisotropy engineering, Sci. Rep. **6**, 31248 (2016).

[52] Christoph Brombacher, Marc Saitner, Christian Pfahler, Alfred Plettl, Paul Ziemann, Denys Makarov, Daniel Assmann, Martin H. Siekman, Leon Abelmann, and Manfred Albrecht, Tailoring particle arrays by isotropic plasma etching: An approach towards percolated perpendicular media, Nanotechnology **20**, 105304 (2009).

[53] M. Heide, G. Bihlmayer, and S. Blügel, Dzyaloshinskii-moriya interaction accounting for the orientation of magnetic domains in ultrathin films: Fe/W(110), Phys. Rev. B **78**, 140403 (2008).

[54] D. Makarov, L. Baraban, I. L. Guhr, J. Boneberg, H. Schift, J. Gobrecht, G. Schatz, P. Leiderer, and M. Albrecht, Arrays of magnetic nanoindentations with perpendicular anisotropy, Appl. Phys. Lett. **90**, 093117 (2007).

[55] D. Makarov, P. Krone, D. Lantiat, C. Schulze, A. Liebig, C. Brombacher, M. Hietschold, S. Hermann, C. Laberty, D. Grosso, and M. Albrecht, Magnetization reversal in arrays of magnetic nanoperforations, IEEE Trans. Magn. **45**, 3515 (2009).

[56] C. Schulze, M. Faustini, J. Lee, H. Schletter, M. U. Lutz, P. Krone, M. Gass, K. Sader, A. L. Bleloch, M. Hietschold, M. Fuger, D. Suess, J. Fidler, U. Wolff, V. Neu, D. Grosso, D. Makarov, and M. Albrecht, Magnetic films on nanoperforated templates: A route towards percolated perpendicular media, Nanotechnology **21**, 495701 (2010).

[57] V. Neu, C. Schulze, M. Faustini, J. Lee, D. Makarov, D. Suess, S.-K. Kim, D. Grosso, L. Schultz, and M. Albrecht, Probing the energy barriers and magnetization reversal processes of nanoperforated membrane based percolated media, Nanotechnology **24**, 145702 (2013).

[58] D. K. Ball, K. Lenz, M. Fritzsche, G. Varvaro, S. Günther, P. Krone, D. Makarov, A. Mücklich, S. Facsko, J. Fassbender, and M. Albrecht, Magnetic properties of granular CoCrPt:SiO_2 thin films deposited on GaSb nanocones, Nanotechnology **25**, 085703 (2014).

[59] D. K. Ball, S. Günther, M. Fritzsche, K. Lenz, G. Varvaro, S. Laureti, D. Makarov, A. Mücklich, S. Facsko, M. Albrecht, and J. Fassbender, Out-of-plane magnetized cone-shaped magnetic nanoshells, J. Phys. D: Appl. Phys. **50**, 115004 (2017).

[60] T. C. Ulbrich, D. Makarov, G. Hu, I. L. Guhr, D. Suess, T. Schrefl, and M. Albrecht, Magnetization Reversal in a Novel Gradient Nanomaterial, Phys. Rev. Lett. **96**, 077202 (2006).

[61] Robert Streubel, Volodymyr P. Kravchuk, Denis D. Sheka, Denys Makarov, Florian Kronast, Oliver G. Schmidt, and

Yuri Gaididei, Equilibrium magnetic states in individual hemispherical permalloy caps, Appl. Phys. Lett. **101**, 132419 (2012).

[62] Robert Streubel, Denys Makarov, Florian Kronast, Volodymyr Kravchuk, Manfred Albrecht, and Oliver G. Schmidt, Magnetic vortices on closely packed spherically curved surfaces, Phys. Rev. B **85**, 174429 (2012).

[63] A. M. Kosevich, B. A. Ivanov, and A. S. Kovalev, Magnetic solitons, Phys. Rep. **194**, 117 (1990).

[64] A. A. Belavin and A. M. Polyakov, Metastable states of a 2D isotropic ferromagnet, JETP Lett. **22**, 245 (1975) .